MBoC | ARTICLE

Common formin-regulating sequences in Smy1 and Bud14 are required for the control of actin cable assembly in vivo

Julian A. Eskin, Aneliya Rankova, Adam B. Johnston, Salvatore L. Alioto, and Bruce L. Goode*
Department of Biology, Rosenstiel Basic Medical Sciences Research Center, Brandeis University, Waltham, MA 02454

ABSTRACT **Formins comprise a large family of proteins with diverse roles in remodeling the actin cytoskeleton. However, the spatiotemporal mechanisms used by cells to control formin activities are only beginning to be understood. Here we dissected Smy1, which has dual roles in regulating formins and myosin. Using mutagenesis, we identified specific sequences in Smy1 critical for its in vitro inhibitory effects on the FH2 domain of the formin Bnr1. By integrating *smy1* alleles targeting those sequences, we genetically uncoupled Smy1's functions in regulating formins and myosin. Quantitative imaging analysis further demonstrated that the ability of Smy1 to directly control Bnr1 activity is crucial in vivo for proper actin cable length, shape, and velocity and, in turn, efficient secretory vesicle transport. A Smy1-like sequence motif was also identified in a different Bnr1 regulator, Bud14, and found to be essential for Bud14 functions in regulating actin cable architecture and function in vivo. Together these observations reveal unanticipated mechanistic ties between two distinct formin regulators. Further, they emphasize the importance of tightly controlling formin activities in vivo to generate specialized geometries and dynamics of actin structures tailored to their physiological roles.**

Monitoring Editor
Laurent Blanchoin
CEA Grenoble

Received: Sep 8, 2015
Revised: Dec 31, 2015
Accepted: Jan 4, 2016

INTRODUCTION

Cells construct a wide range of filamentous actin structures with highly distinct sizes, shapes, dynamics, and architectures (e.g., filopodia, lamellipodia, stress fibers, transport cables, and cytokinetic rings). However, it has remained an open question how such diverse structures with specialized geometries are assembled in cells, often side by side, from a common pool of building blocks. Yeast actin cables provide an excellent model for addressing this question because they are genetically tractable, and despite their extremely dynamic nature, cable length is remarkably well controlled to match the dimensions of the cellular compartment in which they grow. Maintaining the precise length and function of cables is critical for cell viability because the cables serve as tracks for myosin-based transport of essential cargoes destined for the bud tip and cortex (Johnston *et al.*, 1991; Pruyne *et al.*, 1998). As a result, cable overgrowth can lead to misdirected intracellular transport and growth defects (Chesarone *et al.*, 2009; Chesarone-Cataldo *et al.*, 2011).

Yeast actin cables are assembled by two formins, Bni1 and Bnr1 (Evangelista *et al.*, 2002; Sagot *et al.*, 2002; Pruyne *et al.*, 2004), which continuously polymerize cables at extremely fast rates, leading to cable extension in the anterograde direction (from the bud cortex and neck toward the back of the mother cell) at average rates of at least 0.3 μm/s (≥100 subunits/s; Yang and Pon, 2002; Yu *et al.*, 2011). These rapidly growing cables are simultaneously dismantled by the actin disassembly machinery (Okada *et al.*, 2006; Gandhi *et al.*, 2009; Lin *et al.*, 2010). Thus a balance between assembly and disassembly activities governs cable length. In addition, it has been suggested that cable length is influenced by negative feedback mechanisms, including Smy1 control of formin activity (see later discussion; Chesarone-Cataldo *et al.*, 2011; Mohapatra *et al.*, 2015). Cable length may also be affected by mechanisms in place that balance the distribution of actin monomers between competing sets of actin assembly machinery (e.g., formins and Arp2/3 complex; Rotty *et al.*, 2015; Suarez *et al.*, 2015).

---

*Address correspondence to: Bruce L. Goode (goode@brandeis.edu).

Abbreviations used: FH2, formin homology domain 2; GFP, green fluorescent protein; TIRF, total internal reflection fluorescence.

Formins are encoded by 15 different genes in mammals and are essential for a wide range of biological processes, including cell division, cell migration, and cell and tissue morphogenesis (Faix and Grosse, 2006). Using their C-terminal formin homology domains 1 and 2 (FH1 and FH2) and adjacent "tail" sequences, formins directly stimulate actin nucleation, accelerate actin filament elongation, and processively ride the growing barbed ends of filaments while antagonizing capping proteins (Goode and Eck, 2007; Paul and Pollard, 2009). It is believed that the robust actin assembly activities of formins in vivo must be tightly controlled both spatially and temporally in order to build actin arrays of particular sizes and shapes (Chhabra and Higgs, 2007; Chesarone *et al.*, 2010; Breitsprecher and Goode, 2013). However, the full complement of factors regulating formin activities in cells and whether different formin regulators share related mechanisms have been unknown.

In previous work, we identified Bud14 and Smy1 proteins as direct regulators of the yeast formin Bnr1 (Chesarone *et al.*, 2009; Chesarone-Cataldo *et al.*, 2011). We showed that Bud14 localizes to the bud neck with Bnr1 and acts by displacing the FH2 domain of Bnr1 from barbed ends, preventing overgrowth and "buckling" of actin cables in vivo (Chesarone *et al.*, 2009). On the other hand, Smy1 was transiently delivered to Bnr1 at the bud neck and directly inhibited Bnr1 FH2-mediated actin filament elongation; further, *smy1*Δ cells showed distinct defects in actin cable morphology from *bud14*Δ cells (Chesarone-Cataldo *et al.*, 2011). In the present study, we focused initially on suppressor of myosin (Smy1), which is an orphan member of the kinesin superfamily that is most closely related to kinesin-1 but lacks motor activity (Hodges *et al.*, 2009). *SMY1* was first identified as a dosage suppressor of the *myo2-66* temperature-sensitive mutant (Lillie and Brown, 1992) and subsequently was shown to interact with Myo2 through C-terminal sequences in Smy1 (578–657; Figure 1A; Lillie and Brown, 1994, 1998; Beningo *et al.*, 2000). Smy1 also increases the processivity of Myo2 on actin filament bundles in vitro, suggesting a possible mechanism for its suppression of *myo2-66* (Hodges *et al.*, 2009). Independently, Smy1 was identified as a binding partner of Bnr1 (Kikyo *et al.*, 1999), and we later showed that purified Smy1 directly inhibits Bnr1-mediated actin filament elongation (Chesarone-Cataldo *et al.*, 2011). Further, we showed that these activities are contained in a region of Smy1 (421–577) adjacent to, but distinct from, its Myo2-binding site (Figure 1A).

Bnr1 assembles actin cables that fill the mother cell and serve as polarized tracks for myosin V (Myo2)–based traffic of secretory vesicles to the bud (Bretscher, 2003). In our previous work, we showed that Smy1 fused to three copies of green fluorescent protein (Smy1-3xGFP) localizes to secretory vesicles that are transported on cables by Myo2 and that these vesicles pause at the bud neck for 1–2 s before moving into the bud (Chesarone-Cataldo *et al.*, 2011). Further, deletion of *SMY1* led to abnormal actin cable architecture. From these observations, we proposed that Smy1 serves as part of an actin cable length–sensing mechanism, which helps to prevent cable overgrowth and maintains efficient secretory traffic (Chesarone-Cataldo *et al.*, 2011; Mohapatra *et al.*, 2015). However, in the absence of mutants that uncouple the separate interactions of Smy1 with Bnr1 and Myo2, it has not been possible to directly test this model, and it has remained unclear whether the cable defects observed in *smy1*Δ cells result from the loss of Smy1 interactions with Bnr1 or Myo2.

RESULTS

Identification of sequences in Smy1 required for inhibition of Bnr1-mediated actin assembly in vitro

To dissect Smy1 function, we introduced alanine substitutions at conserved sequences in the C-terminal fragment of Smy1 (421–577) that inhibits (or "dampens") the Bnr1 FH2 domain (Chesarone-Cataldo *et al.*, 2011), producing nine new alleles (Figure 1A). Wild-type and mutant Smy1 proteins (421–577) were expressed and purified from *Escherichia coli* and compared in bulk assays over a range of concentrations for their effects on Bnr1(FH2)-mediated actin assembly. Wild-type Smy1 inhibited Bnr1 with half-maximal effects (K_{app}) at 30 nM (Figure 1, B and C). Most of the mutants were found to have a K_{app} similar to that of wild-type Smy1 and were classified as "pseudo wild-type" alleles. However, *smy1-1*, *smy1-4*, and *smy1-7* were 15-fold, >45-fold, and 9.5-fold less potent in inhibiting Bnr1, respectively (Figure 1C).

We next asked how *smy1-1*, *smy1-4*, and *smy1-7* specifically affect the dampening activity of Smy1 on Bnr1-mediated actin filament elongation. Using total internal reflection fluorescence (TIRF) microscopy, we directly monitored the polymerization of individual Oregon green–labeled actin filaments in the presence of Bnr1(FH1-FH2-tail) and profilin with and without wild-type or mutant Smy1 proteins (Supplemental Movie S1). The measured elongation rates of individual filaments are plotted in Figure 1D. Filaments in control reactions lacking Bnr1 elongated at ~10 subunits $s^{-1}\mu M^{-1}$, whereas in reactions containing 100 pM Bnr1(FH1-FH2-tail), a second and faster population of filaments appeared, which elongated at 30–40 subunits $s^{-1}\mu M^{-1}$ (Figure 1D). Addition of wild-type Smy1 (421–577) to these reactions markedly reduced the elongation rate of the second population of filaments to 15–20 subunits $s^{-1}\mu M^{-1}$. By comparison, Smy1-1, Smy1-4, and Smy1-7 had minimal effects in decreasing the rate of filament elongation.

Integrated *smy1* alleles uncouple Smy1 regulation of Bnr1 and Myo2 in vivo

To study the effects of the *smy1* alleles in vivo, we integrated full-length *smy1-1*, *smy1-4*, and *smy1-7* at the *SMY1* locus, generating untagged and 3xGFP-tagged alleles. Each mutant showed expression levels similar to that of wild-type Smy1-3xGFP, with *smy1-1*–3xGFP only slightly less abundant (Figure 2A). Further, GFP fluorescence was localized to puncta that correspond to secretory vesicles (Figure 2B), as previously observed (Chesarone-Cataldo *et al.*, 2011; Hodges *et al.*, 2009). We also compared the spatial distribution patterns of Smy1-3xGFP puncta in wild-type and mutant cells and found that they are not statistically different, and in each case, they are enriched in the bud, and particularly at the bud tip (Figure 2C). Smy1-1–3xGFP displayed a minor enrichment at the bud tip compared with wild-type Smy1-3xGFP, but we do not understand the significance of this. However, because it showed no difference in abundance at the bud neck compared with wild-type Smy1-3xGFP, we included it in further analysis.

We compared cable architecture in fixed wild-type, *smy1*Δ, *smy1-1*, *smy1-4*, and *smy1-7* cells (without GFP tags). Cables in wild-type cells tended to follow smoothly the contours of the mother cortex. In contrast, in *smy1*Δ, *smy1-1*, *smy1-4*, and *smy1-7* cells, some cables were hyperelongated and "wavy," appearing to change direction more frequently (Figure 2D, blue arrowheads). Thus *smy1* alleles defective in Bnr1 regulation phenocopy *smy1*Δ cable defects.

These new *smy1* alleles were designed with the aim of disrupting the Bnr1-regulatory domain of Smy1 (421–577) while avoiding the Myo2-interacting site (578–657) that mediates suppression of *myo2-66*, a mutant with impaired Myo2 motor activity. To test genetically for separation of function, we compared wild-type *SMY1* and mutant *smy1* alleles on high-copy plasmids for their ability to suppress the temperature sensitivity of *myo2-66*. Each *smy1* allele

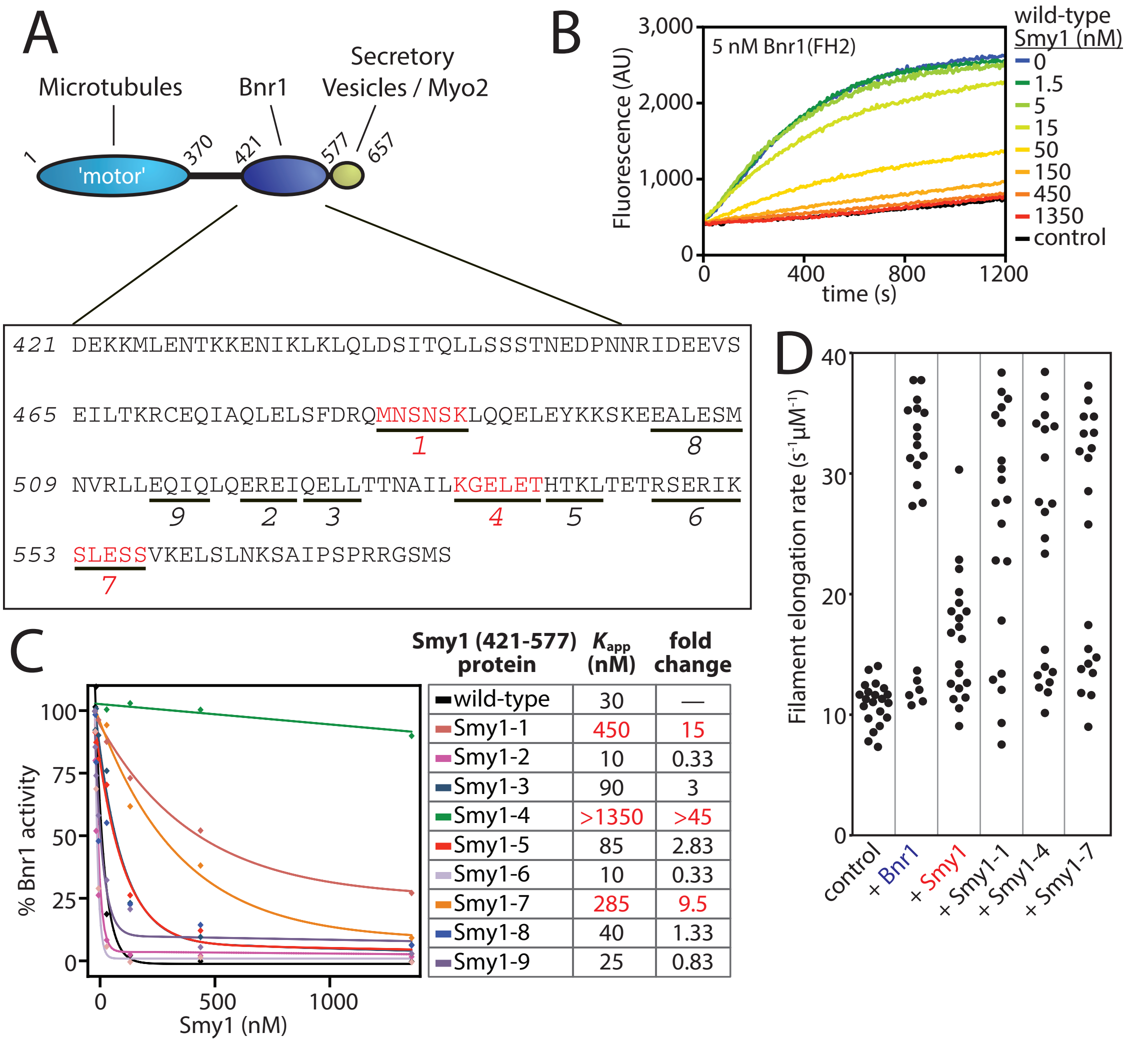

421 DEKKMLENTKKENIKLKLQLDSITQLLSSSTNEDPNNRIDEEVS

465 EILTKRCEQIAQLELSFDRQMNSNSKLQQELEYKKSKEEALESM
1 8

509 NVRLLEQIQLQEREIQELLTTNAILKGELETHTKLTETRSERIK
9 2 3 4 5 6

553 SLESSVKELSLNKSAIPSPRRGSMS
7

Smy1 (421-577) protein	K_{app} (nM)	fold change
▬ wild-type	30	—
▬ Smy1-1	450	15
▬ Smy1-2	10	0.33
▬ Smy1-3	90	3
▬ Smy1-4	>1350	>45
▬ Smy1-5	85	2.83
▬ Smy1-6	10	0.33
▬ Smy1-7	285	9.5
▬ Smy1-8	40	1.33
▬ Smy1-9	25	0.83

FIGURE 1: Dissection of the formin-regulatory domain of Smy1. (A) Smy1 domains with their known physical interactions indicated by solid lines. Boxed below is the sequence of the Bnr1-inhibitory region (421–577) of Smy1, with the residues mutated in each allele underlined. Red indicates alleles found to be defective in Bnr1 inhibition. (B) Monomeric actin (2 µM, 5% pyrene-labeled) was polymerized in the presence of 5 nM Bnr1(FH2) and the indicated concentrations of wild-type Smy1 (421–577). (C) Rates of actin assembly, determined from curves as in B, were plotted as a function of the concentration of wild-type or mutant Smy1 (421–577). Lines are fits to the equation $Y = -100c/(c + K_{app}) + 100$, in which Y is the percentage of remaining Bnr1 activity, c is the molar concentration of Smy1 (421–577), and K_{app} is the apparent binding dissociation constant (nM). Right, table giving K_{app} for wild-type and mutant Smy1 fragments, with the most defective alleles highlighted in red. (D) Elongation rates of individual filaments in TIRF reactions with and without 500 nM wild-type or mutant Smy1 (421–577); $n = 20$ filaments per reaction condition. Reactions performed in two independent trials.

suppressed *myo2-66* to the same extent as wild-type *SMY1* (Figure 2E), and this effect was confirmed for *smy1-4* by measuring cell doubling rates (Figure 2F). Although *myo2-66* bears a mutation in the myosin motor domain, wild-type *SMY1* can additionally suppress *myo2* tail-domain mutants that have cargo-binding defects (Schott *et al.*, 1999). Therefore we tested whether *smy1-1*, *smy1-4*, and *smy1-7* could suppress the temperature sensitivity of *myo2-16*, a tail-domain mutant with cargo-binding defects (Schott *et al.*, 1999). As with *myo2-66*, each *smy1* allele suppressed *myo2-16* to the same extent as wild-type *SMY1* (Figure 2G). Thus the *smy1-1*, *smy1-4*, and *smy1-7* alleles remain functional for Myo2 regulation, demonstrating that Smy1's function in regulating Bnr1-mediated actin cable assembly is independent of its myosin regulatory interactions.

Smy1–Bnr1 interactions are required in vivo for proper actin cable length, architecture, and dynamics

Next we sought to describe more quantitatively the cable defects in mutant cells, focusing our comparison on wild-type, *smy1*Δ, and *smy1-4* cells, since Smy1-4 showed the strongest defects in Bnr1 regulation in vitro. We manually traced 60 cables from each strain with ImageJ (example traces in Figure 3A) and used custom software written in MATLAB to measure distinct features of cables, including cable length, tortuosity, and velocity.

In wild-type cells, cables were on average 5.37 ± 0.30 µm in length (mean ± SEM; Figure 3B). To relate cable length to the overall geometry of the cells, we also measured the lengths of the mother cells for the same strains (Figure 3C). On average, the distance between the bud neck and the "back" of wild-type mother cells was

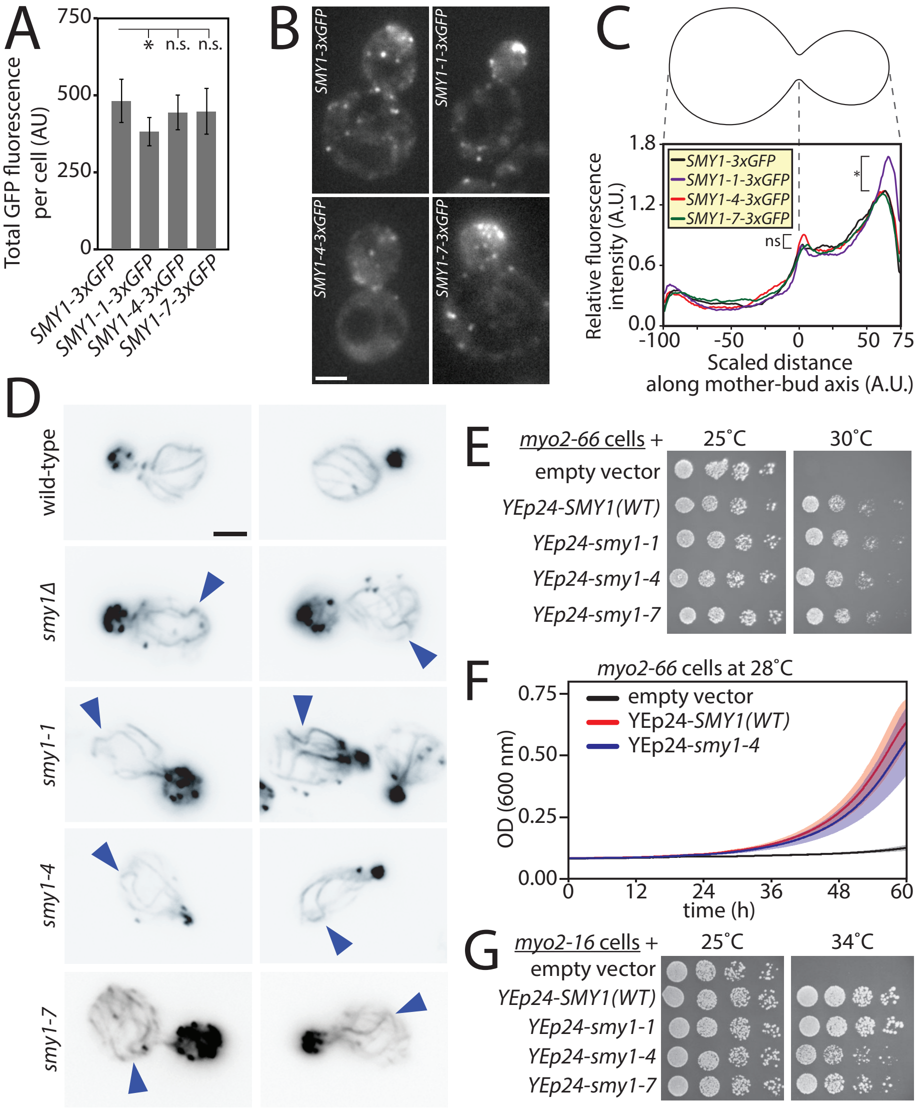

FIGURE 2: *smy1* mutants specifically defective in Bnr1 regulation cause abnormal actin cables. (A) Average Smy1-3xGFP fluorescence levels per cell in the indicated strains. $n > 60$ cells/strain. $*p < 0.0001$. (B) Representative images from strains that have integrated C-terminal 3xGFP tags on wild-type or mutant *SMY1* genes. Scale bar, 2 µm. (C) Images of the spatial distributions of Smy1-3xGFP signal in cells, as in B, were converted to one-dimensional profiles along the mother–bud axis and averaged (see *Materials and Methods*). $n > 60$ cells/strain. Error bars (not shown) obscure the observation that the fluorescence intensity profiles are similar for wild-type and mutant Smy1-3xGFP strains. There was no significant difference between mutant and wild-type distributions, as measured by the Kolmogorov–Smirnov statistical test. However, a Student's *t* test specifically comparing the peaks of wild-type and *SMY1-1–3xGFP* distributions revealed the indicated statistical difference. $*p < 0.05$. (D) Representative cell images showing actin cable organization for the indicated strains. Cells were grown to log phase at 25°C in YEPD and then fixed and stained with Alexa Fluor 488–phalloidin. Image colors were inverted. Blue arrowheads highlight abnormally long or wavy cables. Scale bar, 2 µm. (E) Serial dilutions of *myo2-66* cells carrying the indicated plasmids were plated on selective medium and grown for 3 d at 25 or 30°C. (F) Growth curves of *myo2-66* cells carrying the indicated plasmids grown at 28°C. Curves are averages of 12 duplicates/strain. Lighter shading, SD. Cells were grown in selective liquid medium with shaking in a microplate absorbance reader, and the OD_{600} was measured every 15 min for 60 h. (G) Serial dilutions of *myo2-16* cells carrying the indicated plasmids were plated on selective medium and grown for 3 d at 25 or 34°C.

5.45 ± 0.54 µm. These nearly identical lengths of mother cells and the cables within them suggest that cables extend most of the way through mother cells but typically do not quite reach the distal end of wild-type cells (because of slight cable curvature along the cell cortex). By comparison, in *smy1-4* and *smy1*Δ cells, cables were significantly longer (6.50 ± 0.21 and 6.59 ± 0.19 µm, respectively) than those in wild-type cells (Figure 3B). In particular, *smy1-4* and *smy1*Δ cells each showed an enrichment of cables >7.5 µm in length, consistent with the loss of Bnr1 inhibition.

Using the same cable traces, we measured cable "waviness" or tortuosity, defined as the ratio of a cable's length (*L*) to the distance (*D*) between its two end points. Thus a perfectly straight or direct path would give the minimal value of 1. Wild-type cables had an average tortuosity (*L*/*D* ratio) of 1.29 ± 0.03 (mean ± SEM), consistent with cables following the natural curvature of the cell cortex, but rarely exhibited major bends. In *smy1-4* and *smy1*Δ cells, the average tortuosity of cables was significantly higher (1.41 ± 0.04 and 1.48 ± 0.06, respectively) than in wild-type cells (Figure 3D), suggesting that loss of Smy1 regulation of Bnr1 alters not only cable length but also cable architecture or shape.

We also considered whether mutant defects in cable shape might be related to differences in the size of the mother cell compartment in which they are formed. However, we found that the mother cell lengths were indistinguishable for wild-type, *smy1*Δ, and *smy1-4* cells (Figure 3C). To consider scaling mechanisms more broadly, we asked whether in wild-type cells cable length correlates with mother cell size by comparing cable lengths in haploid (smaller) and diploid (larger) cells. Here we observed that indeed cables are significantly longer in diploid than in haploid cells (Figure 3E). On the other hand, the ratio of cable length to mother cell length was not significantly different between haploid (0.91 ± 0.02) and diploid (0.96 ± 0.03) cells (Figure 3F). Thus cables in wild-type cells (haploid or diploid) on average grow to a length that approaches the length of the cell. Of importance, most of the cables with a length ratio >1.0 (Figure 3F) are not actually "overgrown," because of the gentle curvature of their growth paths along the ellipsoidal mother cell cortex. Similarly, cable tortuosity was not significantly different between haploid and diploid cells (Figure 3G). Thus cable length scales with cell size, but cable shape does not change, as long as the length is properly regulated (e.g., by Smy1).

Although tortuosity is a useful measurement of cable convolutedness, it could stem either from the cable growth path changing direction multiple times (zigzagging) or from the cable tip growing past the rear of the cell and extending back toward the bud neck (looping). To distinguish between these two possibilities, we developed custom software to measure the number of times each cable changed direction along its length (see *Materials and Methods*). This analysis revealed that cables in wild-type cells rarely change direction more than twice along their length, whereas cables in *smy1-4* and *smy1Δ* cells change direction more frequently (Figure 3H). These data suggest that the observed quantitative differences in tortuosity arise from cable "waviness," a phenotype that until now had only been qualitatively described (Chesarone-Cataldo *et al.*, 2011).

Finally, we measured the extension dynamics (velocities) of cables in live cells by spinning-disk confocal microscopy, using an integrated Abp140-3xGFP marker (Yu *et al.*, 2011; Yang and Pon, 2002). To quantify extension rates, we tracked the tips of elongating cables and measured their displacement over time (Supplemental Movie S2). In *smy1-1*, *smy1-4*, *smy1-7*, and *smy1Δ* cells, the mean cable extension velocity was significantly faster than in wild-type cells (Figure 3I), and the mutants all showed an absence of the slowest-growing cables (<0.125 µm/s). By performing this analysis, we also confirmed in real time that some cables in mutant cells visibly change direction upon hitting the cortex (Supplemental Movie S2; *smy1-1* cell). Together these data show that *smy1* mutations that disrupt Bnr1 regulation produce cables with abnormally fast extension rates, which correlates with abnormally long and bent cable shapes.

Smy1 regulation of Bnr1 activity is required for efficient secretory vesicle traffic

To understand how the defects in actin cable architecture and dynamics caused by *smy1* alleles affect polarized secretion, we compared movements of GFP-Sec4 vesicles in the mother compartments of live wild-type and *smy1* mutant cells (Supplemental Movie S3). Examples of GFP-Sec4 particle tracking are shown in Figure 4A. We first measured the directionality of GFP-Sec4 movements in cells during a short (5 s) observation window (Figure 4B). *smy1Δ* cells showed a significant increase in misdirected particle movements compared with wild-type cells, with movements either away from the bud or perpendicular to the mother–bud axis. Similarly, *smy1-1*, *smy1-4*, and *smy1-7* mutants each displayed higher levels of misdirected vesicle movements. Second, we measured the fraction of GFP-Sec4 particles in each mother cell that successfully reached the bud neck during a longer (30 s) observation window (Figure 4C). In *smy1-1*, *smy1-4*, and *smy1-7* mutants, as in *smy1Δ* cells, the "success rate" was substantially lower than in wild-type cells. These observations demonstrate that Smy1–Bnr1 interactions are critical for efficient secretory vesicle traffic.

In addition, we tracked the paths of secretory vesicle transport in wild-type and *smy1* mutant cells and measured the tortuosity of these paths (Figure 4D; example tracks in Figure 4A). Secretory paths had a much lower *L/D* ratio in wild-type than in *smy1* mutant cells, indicating that secretory transport is more circuitous in *smy1* mutants. In particular, a larger fraction of vesicles in the mutant cells followed paths with a tortuosity >1.5, although many of the vesicles also followed "normal" paths. Thus vesicle path tortuosity distributions mirrored cable tortuosity distributions in the same strains (Figure 3D), also explaining the observed inefficiency of secretory traffic in the mutants.

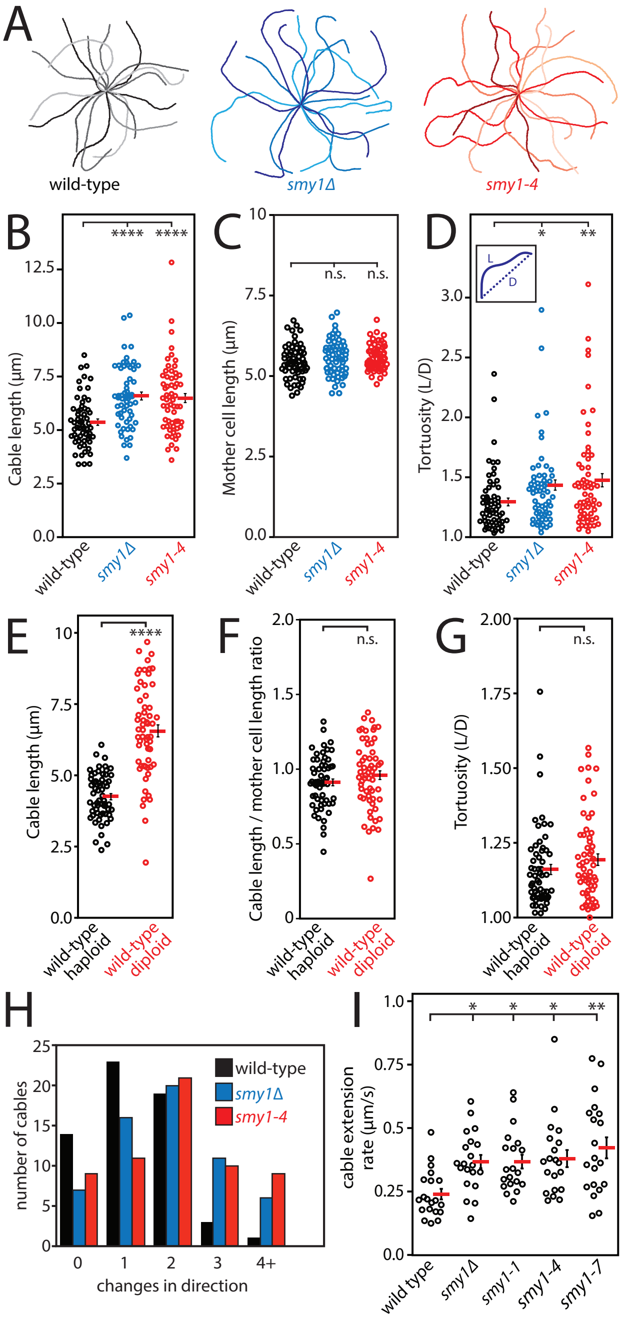

FIGURE 3: In vivo defects in actin cable length, shape, and dynamics in *smy1* mutants. (A) Cables stained with Alexa Fluor 488–phalloidin in the indicated strains were traced using ImageJ ($n = 60$ cables/strain). Eighteen representative traces of cables in each strain are displayed in a radial array around the position of the bud neck for each trace. (B) Lengths of individual cable traces. Red bars, means. Error bars, SEM. $n = 60$ per strain. ****$p < 0.0001$. (C) Lengths of individual mother cells from the same images used in A and B, measured in ImageJ as the distance between the bud neck and the furthest point in the mother cell. (D) Tortuosity (ratio of length, *L*, to distance, *D*, between end points) of individual cable traces. Red bars, means. Error bars, SEM. $n = 60$ per strain. *$p = 0.0208$. (E) Lengths of individual cable traces from images of the indicated strains stained with Alexa Fluor 488–phalloidin. Red bars, means. Error bars, SEM. $n = 60$ per strain. ****$p < 0.0001$. (F) Ratios of the actin cable lengths in E to the corresponding mother cell lengths measured as in C. Red bars: means. Error bars, SEM. $n = 60$ cells/strain. **(G)** Tortuosity (*L/D* ratio) of individual cable traces. Red bars, means. Error bars, SEM. $n = 60$ per strain. (H) Number of cables exhibiting the indicated numbers of changes in direction, defined as a change of at least 10° within 0.5-µm cable length. $n = 60$ per strain. (I) Rates of cable extension, determined from live imaging of Abp140-3xGFP dynamics. Red bars, means. Error bars, SEM. *$p < 0.05$ and **$p < 0.01$.

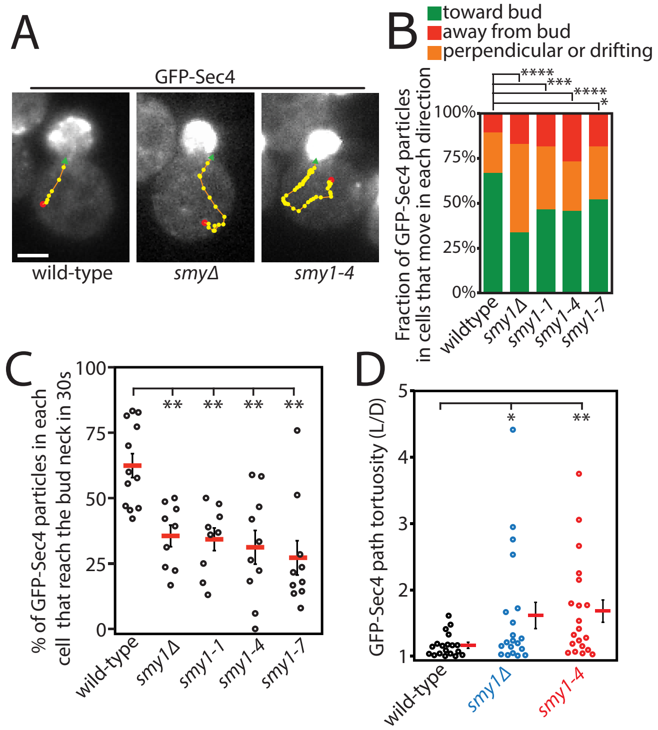

FIGURE 4: Defects in polarized secretory vesicle traffic in *smy1* mutants. (A) Initial frames from representative time-lapse movies showing GFP-Sec4 in the indicated strains. Yellow dots correspond to the position of a single GFP-Sec4 particle in successive frames, from its first appearance to its arrival at the bud neck; red dot, initial frame; green arrowhead, final frame. Scale bar, 2 μm. (B) Directionality of GFP-Sec4 particle movements observed in the indicated strains. Puncta were categorized as moving anterograde (rapid vectoral movement toward the bud), retrograde (vectoral movement away from the bud), or perpendicular to the mother–bud axis and/or nonvectoral "drifting." $n = 75$ particles/strain. The distributions of these data were tested for statistical differences between strains using the Pearson's chi-squared test. *$p = 0.0151$, ***$p < 0.001$, ****$p < 0.0001$. (C) Fraction of GFP-Sec4 particles that reached the bud neck within a 30-s observation window. Each dot is the fraction of particles successfully trafficked in one cell; 8–15 GFP-Sec4 puncta scored per cell. **$p < 0.01$ by one-way ANOVA. Red bars, means. Error bars, SEM. (D) Paths of individual GFP-Sec4 puncta were tracked. Tortuosity (L/D) of individual paths. Red bars, means. Error bars, SEM. $n = 20$ per strain. *$p < 0.05$ and **$p < 0.01$.

A "Smy1-like" motif in Bud14 is critical for its role in actin cable regulation in vivo

To identify other proteins in the *Saccharomyces cerevisiae* proteome with potential roles in formin regulation, we performed BLAST searches (http://blast.ncbi.nlm.nih.gov) using each of the formin-regulatory motifs in Smy1 as queries. These searches yielded numerous hits, as expected for short queries, and therefore we applied an additional filter, selecting proteins linked to the cytoskeleton by gene ontology (GO) and only those with motifs at least 80% identical to the query. By these criteria, we identified Bud14, Uso1, and Dad1. Among these hits, Bud14 stood out because it is a known inhibitor of Bnr1 (Chesarone *et al.*, 2009). However, Bud14 was also a surprising hit because it has no similarity to Smy1 in overall sequence or domain layout (Figure 5A) and its biochemical and genetic effects on Bnr1 are distinct from those of Smy1 (Chesarone *et al.*, 2009). To test the importance of the Smy1-like motif in Bud14 in actin cable regulation in vivo, we compared the abilities of low-copy (CEN) plasmids expressing wild-type *BUD14* or *bud14-1* (analogous to *smy1-1*, with alanine substitutions at five residues, 135 and 137–140; Figure 5A) under control of the *BUD14* promoter to complement defects in cable formation and secretory vesicle transport in *bud14Δ* cells (Chesarone *et al.*, 2009). This analysis showed that *bud14Δ* cells carrying empty control vector have hyperelongated and buckled cables (Figure 5B, blue arrowheads) that are rescued by a *BUD14* plasmid but not a *bud14-1* plasmid.

To quantify the cable defects in *bud14-1* mutants, we scored cells for the presence of abnormally bent or buckled cables, defined as those that change in direction by >90° at the cell cortex (Figure 5C). By this metric, *bud14Δ* cells covered by the *bud14-1* plasmid had a cable phenotype indistinguishable from that of *bud14Δ* cells covered by empty vector, whereas the *BUD14* plasmid fully rescued the defects. To assess cable "overgrowth," we measured F-actin intensity in the distal one-third of the mother cell (farthest from the bud neck), quantified as a fraction of the entire mother cell, and computed the probability distributions (Figure 5D). In this analysis, cells were imaged with a shorter exposure time to avoid saturating the fluorescence signal (as in Figure 5D, inset). In *bud14Δ* cells covered by a *BUD14* plasmid, the distribution was nearly identical to that of wild-type cells. However, for *bud14Δ* cells covered by a *bud14-1* plasmid, the F-actin distribution was shifted toward the rear of the cell, similar to that of the empty vector. Further, using live-cell imaging, we asked whether the cables in cells expressing *bud14-1* support efficient secretory traffic, by measuring the fraction of secretory vesicles (GFP-Sec4) in the mother cell that reached the bud neck during a 30-s observation window (Figure 5E and Supplemental Movie S4). Vesicles in *bud14Δ* cells covered by empty vector or *bud14-1* showed markedly reduced efficiency of traffic and displayed circuitous paths of movement, sometimes retrograde instead of anterograde.

These results, together with our previous observations (Chesarone *et al.*, 2009; Chesarone-Cataldo *et al.*, 2011), demonstrate that the formin regulatory effects of Smy1 and Bud14 are each required for the proper control of actin cable length, shape, and function. To test whether the loss of Smy1 and Bud14 activities together leads to additive cable defects, we compared cable length distributions for wild-type, *smy1Δ*, *bud14Δ*, and *smy1Δbud14Δ* cells (Figure 5F). As expected, *smy1Δ* and *bud14Δ* cables were each significantly longer than wild-type cables; however, the cables in *smy1Δbud14Δ* cells were no longer than in either single mutant. Further, *smy1Δbud14Δ* double-mutant cells showed similar defects in cable tortuosity to those of *smy1Δ* and *bud14Δ* single mutants (Figure 5G). These results were unexpected, given that *smy1Δ* and *bud14Δ* mutations show compounded defects in cell growth (Chesarone-Cataldo *et al.*, 2011), and require further mechanistic investigation to understand.

DISCUSSION

In this work, we defined three sequence motifs in Smy1 required both for its ability to regulate formin (Bnr1) FH2 domain activities in vitro and for its cellular functions in regulating actin cable formation and secretory traffic. By targeting these motifs with point mutations, we were able to uncouple Smy1 in vivo functions in regulating Bnr1 and Myo2 and demonstrate for the first time that the loss of Smy1 effects on Bnr1 leads to defective actin cable architecture and dynamics, independent of Smy1 effects of Myo2. These observations made it clear that Smy1 is a multifunctional protein, controlling both the formation of the actin track itself (via interactions with the formin) and the activity of the motor that transports cargo along the track.

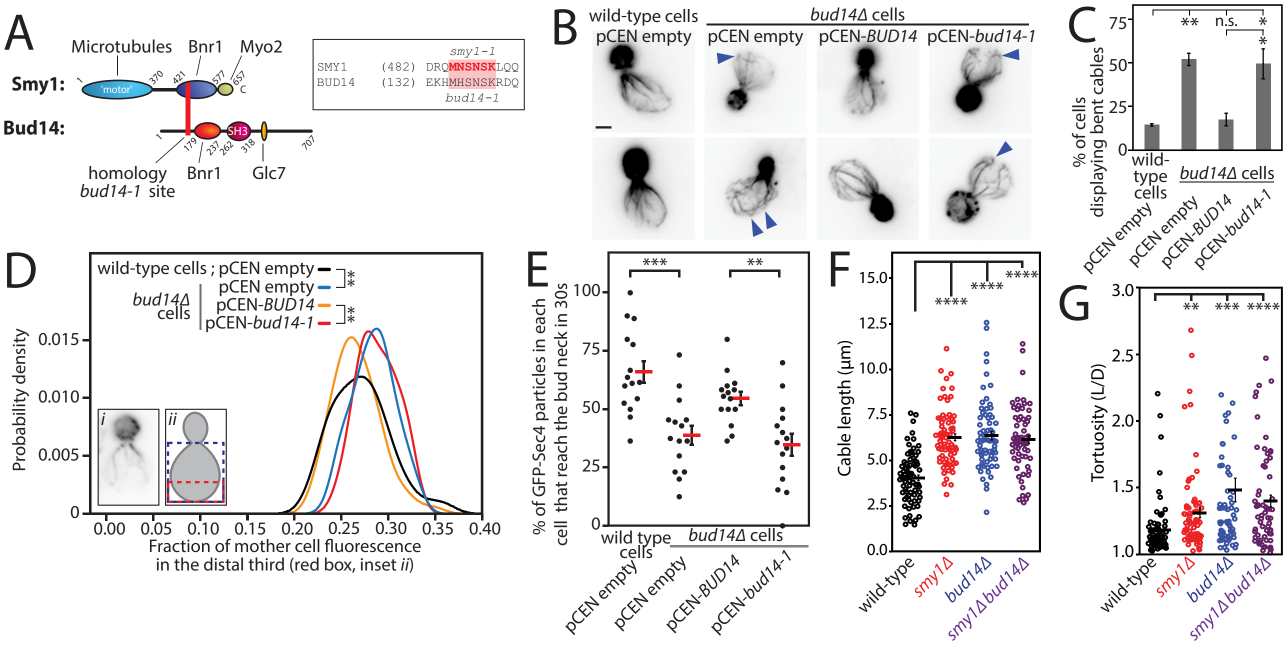

FIGURE 5: Bud14 in vivo functions in regulating actin cable formation and promoting secretory traffic depend on its Smy1-like motif. (A) Domain layouts of Smy1 and Bud14, highlighting similar motifs. The motif in Bud14 is highly similar to the motif defined by *smy1-1*. (B) Representative cell images showing actin cable architecture. Cells were grown to log phase at 25°C in YEPD, fixed, and stained with Alexa Fluor 488–phalloidin. Image colors are inverted. Blue arrowheads highlight abnormally long or wavy cables. Error bars, SD. Scale bar, 2 µm. (C) Fraction of cells containing at least one misshapen cable. Cables displaying a curve of >90° from the cell cortex were scored as bent. $n = 200$ cells/strain in two independent experiments. (D) Probability distributions of F-actin fluorescence in cells. Images as in B were acquired with lower exposure time (200 ms) to avoid saturated signal. Within each mother cell ($n = 50$ cells/ strain), the fraction of fluorescence signal observed within the distal one-third of the cell (inset ii, red box) was measured using custom MATLAB code. (E) Fraction of GFP-Sec4 particles in the indicated strains that reached the bud neck within a 30-s observation window. Each dot represents the fraction of vesicles successfully transported in one cell; 10–15 GFP-Sec4 puncta were scored per cell. Red bars, means. Error bars, SEM. $n = 15$ cells/strain. (F) Lengths of individual cable traces from images of the indicated strains stained with Alexa Fluor 488–phalloidin. Black bars, means. Error bars, SEM. $n = 70$ per strain. ****$p < 0.0001$. (G) Tortuosity (L/D ratio) of individual cable traces. Black bars, means. Error bars, SEM. $n = 70$ per strain. **$p < 0.01$, ***$p < 0.001$, and ****$p < 0.0001$.

In our previous work on Smy1 (Chesarone-Cataldo *et al.*, 2011), we provided a primarily descriptive comparison of actin cables in wild-type and *smy1Δ* cells. Here we defined more quantitatively the alterations in actin cable shape and velocity caused by loss of Smy1 interactions with Bnr1 and correlated these cable defects with a reduced efficiency in secretory vesicle traffic. Importantly, by all quantitative criteria that we measured for cable morphology and function, *smy1-4* was at least as defective as *smy1Δ*. These observations also provide new support for a recently described cable length control mechanism involving myosin and Smy1 (Chesarone-Cataldo *et al.*, 2011; Mohapatra *et al.*, 2015), in which the delivery rate of Smy1 particles (secretory vesicles) on cables scales with cable length and thus selectively inhibits the growth of longer cables, preventing cable overgrowth. Quantitative modeling of this mechanism predicts that mutations disrupting Smy1-formin interactions should lead to abnormally fast-growing and long cables in cells (Mohapatra *et al.*, 2015), which is confirmed by our observations here.

In parallel, we measured the lengths of mother cells to show that *smy1* mutant cable shape defects arise not from a shortening of the cellular compartment but instead from overgrowth or "hyperextension" of cables. Further, our comparison of smaller and larger (haploid and diploid, respectively) wild-type cells indicates that in general, cable length scales with cell size, but cable shape remains normal as long as there is a length control mechanism (such as Smy1) in place. We envision two possible mechanisms by which the mutant defects in cable shape might arise: 1) cables might buckle upon colliding with the cell cortex as a result of overgrowth, and 2) cable architecture and shape might be compromised earlier in growth, well before cables reach the cortex, possibly as a result of the elevated cable extension rates in these mutants. Discerning between these and other possible mechanisms will require further live imaging analysis of cables.

Our results expose an intriguing and unanticipated parallel between the mechanisms of formin regulation by Smy1 and Bud14, tied together by their dependence on common sequence motifs (mutated in *smy1-1* and *bud14-1*). This is interesting, because both proteins bind directly to the FH2 domain of Bnr1, yet they have distinct effects on Bnr1 activity in vitro and lead to distinct mutant cable phenotypes in vivo (Chesarone *et al.*, 2009; Chesarone-Cataldo *et al.*, 2011). Thus Smy1 and Bud14 appear to use related mechanisms to interact with the FH2 domain, yet they differentially control formin activity. We speculate that the differences in their effects on Bnr1 activity might be due to differences in their protein structures and/or the other contacts they make with the FH2 domain. Of importance, only the *smy1-1* motif was conserved in Bud14 and not the *smy1-4* or *smy1-7* motifs, and other sequences in Bud14 that mediate its effects on Bnr1 activity are not conserved in Smy1 (Chesarone *et al.*, 2009). Thus the broad implications of these results are that common sequence motifs might be used by a variety of formin regulators and that formin regulators might have a modular design in which mixing and matching of different formin-interacting motifs/domains determines their distinct regulatory effects.

Finally, our work highlights the importance of tuning the activities of formins in cells to generate actin networks of a particular size, shape, and dynamics. Although we focused here on the control of formins in building yeast actin cables, related mechanisms might be involved in controlling the formin-mediated assembly of other actin structures with specialized lengths and shapes, such as filopodia, stress fibers, contractile rings, and stereocilia. It is our hope that the mechanisms we uncovered in this study, as well as the methods we used to quantify different physical parameters of yeast actin cables, might apply more broadly to the study of formin regulation in other systems and to the construction of a wide range of actin structures.

MATERIALS AND METHODS

Plasmids and yeast strains

Plasmids for galactose-inducible expression of hexahistidine (6His)-Bnr1(FH1-FH2-tail; 757–1375) in *S. cerevisiae* have been described (Moseley and Goode, 2005; Okada *et al.*, 2010; Jaiswal *et al.*, 2013). Plasmids used for *E. coli* expression and purification of 6His-Smt3-Bnr1(FH2) and 6His-Ulp1 were gifts from Mike Rosen (University of Texas Southwestern Medical Center, Dallas, TX). The *E. coli* expression plasmid for 6His-Smy1(421–577) has been described (Chesarone-Cataldo *et al.*, 2011) and was used as a template to generate alanine substitutions in *SMY1* by site-directed mutagenesis, which were verified by DNA sequencing. Standard methods were used for general molecular biology and yeast work (Sambrook *et al.*, 1989; Guthrie and Fink, 1991). Low-copy (*CEN*) plasmids for expressing *GFP-SEC4* in *S. cerevisiae* and integrating *ABP140-3xGFP::LEU2* have been described (Calero *et al.*, 2003; Buttery *et al.*, 2007). A sibling plasmid for integrating *ABP140-3xGFP::HIS3* was generated by subcloning the *ABP140-3xGFP* cassette into pRS303 (Sikorski and Hieter, 1989) between the *Apa*I and *Not*I restriction sites. A plasmid for integrating *SMY1-3xGFP::LEU2* has been described (Chesarone-Cataldo *et al.*, 2011). From this, integration plasmids for C-terminal 3xGFP-tagged *smy1* alleles were generated by site-directed mutagenesis and verified by restriction pattern and DNA sequencing. Integration plasmids for untagged *smy1* alleles were generated by removing the *3xGFP* sequence by restriction digest with *Bam*HI and *Not*I (New England BioLabs, Ipswich, MA) and replacing it with a short DNA fragment containing an in-frame stop codon. A low-copy (*CEN*) plasmid for expression of *BUD14* was generated by PCR-amplifying the *BUD14* open reading frame plus 300 base pairs of 3′ and 5′ untranslated sequence from wild-type genomic DNA and cloning this sequence into the *Bam*HI and *Not*I sites of pRS316 (Sikorski and Hieter, 1989). A corresponding *bud14-1* plasmid was generated by using site-directed mutagenesis to make alanine substitutions at Bud14 residues 135 and 137–140. The high-copy (*2 µ*) plasmid YEp24-*SMY1* has been described (Marcoux *et al.*, 2000), and corresponding YEp24 plasmids expressing *smy1-1*, *smy1-4*, and *smy1-7* were generated by site-directed mutagenesis of the *SMY1* parent plasmid and verified by DNA sequencing. All yeast strains used in this study were in the W303 background (*leu2-3112; trp1-1; can1-100; ura3-1; ade2-1; his3-11,15*), except *myo2-66* (*ade1; his6; leu2-3112; ura3-52; myo2-66*) and *myo2-16* (*his3Δ200; ura3-52; leu2-3112; lys2-801; ade2-101; myo2-16::HIS3;* Gal+), which were generously provided by Tony Bretscher (Cornell University, Ithaca, NY).

Protein purification

Wild-type and mutant 6His-Smy1(421–577) polypeptides were purified from *E. coli* as described (Chesarone-Cataldo *et al.*, 2011). 6His-Bnr1(FH1-FH2-tail; 757–1375) was purified after Gal overexpression in *S. cerevisiae* as described (Moseley *et al.*, 2006). Untagged Bnr1(FH2; 868-1291) was expressed in *E. coli* and purified as described (Graziano *et al.*, 2013). Rabbit muscle actin was purified and fluorescently labeled with pyrenyl-iodoacetamide or Oregon green on Cys^{374} as described in detail (Graziano *et al.*, 2013). Untagged human profilin was expressed in *E. coli* and purified as previously described for yeast profilin (Moseley *et al.*, 2004).

Bulk actin assembly assays

Kinetics of pyrene-actin assembly were measured as previously described (Graziano *et al.*, 2014). Fluorescence was monitored in a plate reader (Infinite M200; Tecan, Männedorf, Switzerland). Rates of pyrene-actin assembly were determined from the slope of each curve at 50% polymerization, with normalization of each value to that of reactions containing Bnr1 alone (no Smy1). K_{app} was determined by fitting a hyperbolic decay curve (logistic function) to the dose curve for each Smy1 protein and defining the concentration of half-maximal inhibition. Fold change from wild-type Smy1 was calculated by dividing mutant K_{app} by wild-type K_{app}.

Total internal reflection fluorescence microscopy

TIRF microscope setup and conditions used were as described (Graziano *et al.*, 2014). Briefly, coverslips were coated with methoxy-poly-(ethylene glycol)-silane (Laysan Bio, Arab, AL) and assembled into flow cells. Immediately before each experiment, flow cells were incubated for 2 min in HBSA (20 mM 4-(2-hydroxyethyl)-1-piperazineethanesulfonic acid, pH 7.5, 1 mM EDTA, 50 mM KCl, 1% bovine serum albumin) and then washed with TIRF buffer (10 mM imidazole, 50 mM KCl, 1 mM $\mathrm{MgCl_2}$, 1 mM ethylene glycol tetraacetic acid, 0.2 mM ATP, 10 mM dithiothreitol, 15 mM glucose, 20 µg/ml glucose oxidase, and 0.5% methylcellulose [4000 cP], pH 7.4). Proteins in TIRF buffer were then mixed with 0.5 µM G-actin (10% Oregon Green labeled) and added to the flow cell. Images were acquired at 7.5-s intervals for 600 s using an inverted microscope (Ti200; Nikon Instruments, Melville, NY) with a 150-mW argon laser (Melles Griot, Carlsbad, CA), a 60× TIRF objective (numerical aperture [NA] 1.49; Nikon), and an electron-multiplying charge-coupled device (EMCCD) camera (iXon; Andor Technology, South Windsor, CT). Focus was maintained using the Perfect Focus System (Nikon Instruments). Elongation rates of filaments were determined in ImageJ (National Institutes of Health, Bethesda, MD) by measuring the length of each filament at 30-s intervals over a period of at least 300 s.

Quantitative analysis of Smy1-3xGFP expression and localization

Yeast cells were grown to mid log phase (OD_{600} = 0.1–0.3) in rich medium. Immediately before imaging, cells were centrifuged for 5 s at 10,000 × *g*, and 9/10 of the volume was removed. Then cells were gently resuspended in the remaining 1/10 volume of medium. Cells were mounted on a slide with a coverslip and imaged on a Nikon i-E upright epifluorescence microscope equipped with a 100× Plan Apochromat oil immersion objective (NA 1.45; Nikon Instruments) and an Andor Zyla scientific complementary metal-oxide semiconductor detector (Andor Technology) controlled by NIS Elements Advanced Research software (Nikon Instruments). Smy1-3xGFP fluorescence intensity per cell was measured from single focal planes after background subtraction using ImageJ (National Institutes of

Health) and compared between strains. For each strain, the distribution of fluorescence along the mother–bud axis in each of 60 cells was measured using custom software we developed in MATLAB (MathWorks, Natick, MA). This was accomplished by cropping each cell from larger images and manually defining the location of the bud tip, bud neck, and "base" of the mother cell. The mother–bud axis was defined as the line connecting the cell "base" and the bud tip. We calculated a one-dimensional fluorescence intensity profile for each cell along the length of its axis of polarity. The fluorescence value at each point along the profile corresponds to the mean fluorescence intensity of pixels in the cell on a line perpendicular to the axis at that point. We then rescaled the profiles from individual cells by defining the position –100 (in arbitrary units) as the "base" of the mother cell, position 0 as the bud neck, and position +75 as the bud tip, producing an average fluorescence intensity distribution along the mother–bud axis for each strain.

Quantitative analysis of actin cable length and architecture in fixed cells

Yeast cells were grown to mid log phase (OD_{600} = 0.1–0.3) in yeast extract/peptone/dextrose (YEPD) medium (Figure 2D) or synthetic selective medium (Figure 5B) and then fixed in 4.7% formaldehyde for 30–45 min and washed three times with phosphate-buffered saline (PBS). Cells were stained with Alexa Fluor 488–phalloidin (Life Technologies, Grand Island, NY) and then washed again three times with PBS. Cells were imaged in mounting medium (10 mM $NaPO_4$, pH 7.4, 75 mM NaCl, 4.3 mM *p*-phenylenediamine, 0.01 mg/ml 4′,6-diamidino-2-phenylindole, and 45% glycerol [vol/vol]) at 25°C on an Axioskop 2 mot plus microscope (Carl Zeiss, Thornwood, NY) equipped with a 100× Plan Apochromat oil immersion objective, NA 1.40 (Carl Zeiss), and a digital CCD camera (ORCA-ER; Hamamatsu Photonics, Middlesex, NJ). Images were acquired using OpenLab software (PerkinElmer, Waltham, MA) and analyzed using ImageJ) and software custom written in MATLAB. Individual actin cables in cells were manually traced using a stylus on an iPad (Apple, Cupertino, CA) mirroring the computer display. The *xy*-coordinates of trace points were exported from ImageJ into MATLAB to compute their length and the ratio of their length to the distance between cable end points (tortuosity). In addition, we measured the number of changes in direction for each cable trace by defining the direction of curvature (left or right) at each point along the trace and counting the number of inflection points, defining the minimum angle change of a "curve" as 10° per 0.5 µm of cable. To measure the fraction of mother cell fluorescence in the distal one-third of the cell, we manually defined the boundaries of the cell (blue box in Figure 5D, inset) and the bud neck position. Then, we used custom MATLAB code to subdivide the cell and compute the fluorescence fraction in each region. The probability densities shown in Figure 5D were determined from these data, also using MATLAB, as previously described (Chesarone-Cataldo *et al.*, 2011).

Live-cell imaging of actin cable dynamics

Yeast cells were grown to early log phase ($OD_{600} \approx 0.1$) in YEPD medium. Immediately before imaging, cells were centrifuged for 5 s at 10,000 × *g*, and 0.95 of the volume was removed. Then cells were gently resuspended in the remaining 0.05 volume of medium. Cells were mounted on a slide with a coverslip and immediately imaged through a 100× objective and 1.2× magnifier on a Nikon i-E upright confocal microscope equipped with a CSU-W1 spinning-disk head (Yokogawa, Tokyo, Japan) and an Andor Ixon 897 Ultra CCD camera controlled by Nikon NIS-Elements Advanced Research software. A single optical slice was imaged every 80 ms (12.5 frames/s) for 60 s per field. Individual cells were cropped using ImageJ software. Actin cable extension speed and angles (relative to each cell's axis of polarity) were measured using custom software written in MATLAB.

Live-cell imaging and analysis of GFP-Sec4 particle movements

Wild-type and mutant yeast strains transformed with a CEN plasmid expressing GFP-Sec4 were grown to mid log phase ($OD_{600} \approx 0.1$) in synthetic selective medium (2% glucose). Cells were transferred directly from each culture onto a microscope slide and imaged on an inverted microscope (Ti200; Nikon Instruments) equipped with an Intensilight excitation source (Nikon Instruments), 100× objective (NA 1.30; Nikon), 1.5× magnifier, and iXon EMCCD camera (Andor). Focus was maintained using the Perfect Focus System (Nikon Instruments). We acquired 200 ms exposures continuously for 60 s (5 frames/s). Movies were analyzed as follows using ImageJ. When measuring the directionality of secretory vesicle traffic, the positions of individual GFP-Sec4 puncta in cells were manually tracked, and the directionality of their movement was scored as either vectoral toward the bud, away from the bud, or perpendicular to the mother–bud axis and/or nonvectoral drifting. In addition, for each strain, we calculated the fraction of GFP-Sec4 puncta in the mother cell that were successfully transported to the bud neck in a 30-s observation window by tracking 8–15 puncta/cell from at least 10 cell/strain. Statistical differences in the results were determined by one-way analysis of variance (ANOVA). For comparison of the paths taken by secretory vesicles in various strains, individual GFP-Sec4 puncta were tracked from the beginning of vectoral movement until they reached the bud neck. For each path, we then measured the ratio of path length to the distance between path end points (tortuosity).

BLAST homology searching

As queries in our BLAST searches against the *S. cerevisiae* proteome, we used the residues mutated in the *smy1-1*, *smy1-4*, and *smy1-7* alleles (underlined) plus two to four flanking residues: RQMNSNSKLQ, ILKGELETHTK, ERIKSLESSVK. We considered only hits with at least 80% identity to the *smy1-1*, *smy1-4*, or *smy1-7* motif. Further, we considered only those proteins with gene ontology GO annotations that contain the terms actin, microtubule, tubulin, and/or cytoskeleton. GO annotations were downloaded from the *Saccharomyces* Genome Database (as of January 16, 2015).

ACKNOWLEDGMENTS

We are grateful to M. Chesarone-Cataldo for providing guidance on this project and editing the manuscript, to S. W. Bear for unconditional support throughout this work, and to L. Mohapatra and J. Kondev for invaluable discussions on actin cable formation. This project was supported by a grant from the National Institutes of Health (GM083137) to B.G. and by National Science Foundation Materials Research in Science and Engineering Center Grant MRSEC-142038.

REFERENCES

Beningo KA, Lillie SH, Brown SS (2000). The yeast kinesin-related protein Smy1p exerts its effects on the class V myosin Myo2p via a physical interaction. Mol Biol Cell 11, 691–702.

Breitsprecher D, Goode BL (2013). Formins at a glance. J Cell Sci 126, 1–7.

Bretscher A (2003). Polarized growth and organelle segregation in yeast: the tracks, motors, and receptors. J Cell Biol 160, 811–816.

Buttery SM, Yoshida S, Pellman D (2007). Yeast formins Bni1 and Bnr1 utilize different modes of cortical interaction during the assembly of actin cables. Mol Biol Cell 18, 1826–1838.

Calero M, Chen CZ, Zhu W, Winand N, Havas KA, Gilbert PM, Burd CG, Collins RN (2003). Dual prenylation is required for Rab protein localization and function. Mol Biol Cell 14, 1852–1867.

Chesarone M, Gould CJ, Moseley JB, Goode BL (2009). Displacement of formins from growing barbed ends by bud14 is critical for actin cable architecture and function. Dev Cell 16, 292–302.

Chesarone MA, Dupage AG, Goode BL (2010). Unleashing formins to remodel the actin and microtubule cytoskeletons. Nat Rev Mol Cell Biol 11, 62–74.

Chesarone-Cataldo M, Guérin C, Yu JH, Wedlich-Söldner R, Blanchoin L, Goode BL (2011). The myosin passenger protein Smy1 controls actin cable structure and dynamics by acting as a formin damper. Dev Cell 21, 217–230.

Chhabra ES, Higgs HN (2007). The many faces of actin: matching assembly factors with cellular structures. Nat Cell Biol 9, 1110–1121.

Evangelista M, Pruyne D, Amberg DC, Boone C, Bretscher A (2002). Formins direct Arp2/3-independent actin filament assembly to polarize cell growth in yeast. Nat Cell Biol 4, 32–41.

Faix J, Grosse R (2006). Staying in shape with formins. Dev Cell 10, 693–706.

Gandhi M, Achard V, Blanchoin L, Goode BL (2009). Coronin switches roles in actin disassembly depending on the nucleotide state of actin. Mol Cell 34, 364–374.

Goode BL, Eck MJ (2007). Mechanism and function of formins in the control of actin assembly. Annu Rev Biochem 76, 593–627.

Graziano BR, Jonasson EM, Pullen JG, Gould CJ, Goode BL (2013). Ligand-induced activation of a formin-NPF pair leads to collaborative actin nucleation. J Cell Biol 201, 595–611.

Graziano BR, Yu H-YE, Alioto SL, Eskin JA, Ydenberg CA, Waterman DP, Garabedian M, Goode BL (2014). The F-BAR protein Hof1 tunes formin activity to sculpt actin cables during polarized growth. Mol Biol Cell 25, 1730–1743.

Guthrie C, Fink GR (eds.) (1991). Guide to Yeast Genetics and Molecular Biology, San Diego, CA: Academic Press.

Hodges AR, Bookwalter CS, Krementsova EB, Trybus KM (2009). A nonprocessive class V myosin drives cargo processively when a kinesin- related protein is a passenger. Curr Biol 19, 2121–2125.

Jaiswal R, Breitsprecher D, Collins A, Corrêa IR, Xu M-Q, Goode BL (2013). The formin Daam1 and fascin directly collaborate to promote filopodia formation. Curr Biol 23, 1373–1379.

Johnston GC, Prendergast JA, Singer RA (1991). The Saccharomyces cerevisiae MYO2 gene encodes an essential myosin for vectorial transport of vesicles. J Cell Biol 113, 539–551.

Kikyo M, Tanaka K, Kamei T, Ozaki K, Fujiwara T, Inoue E, Takita Y, Ohya Y, Takai Y (1999). An FH domain-containing Bnr1p is a multifunctional protein interacting with a variety of cytoskeletal proteins in Saccharomyces cerevisiae. Oncogene 18, 7046–7054.

Lillie SH, Brown SS (1992). Suppression of a myosin defect by a kinesin-related gene. Nature 356, 358–361.

Lillie SH, Brown SS (1994). Immunofluorescence localization of the unconventional myosin, Myo2p, and the putative kinesin-related protein, Smy1p, to the same regions of polarized growth in Saccharomyces cerevisiae. J Cell Biol 125, 825–842.

Lillie SH, Brown SS (1998). Smy1p, a kinesin-related protein that does not require microtubules. J Cell Biol 140, 873–883.

Lin MC, Galletta BJ, Sept D, Cooper JA (2010). Overlapping and distinct functions for cofilin, coronin and Aip1 in actin dynamics in vivo. J Cell Sci 123, 1329–1342.

Marcoux N, Cloutier S, Zakrzewska E, Charest PM, Bourbonnais Y, Pallotta D (2000). Suppression of the profilin-deficient phenotype by the RHO2 signaling pathway in Saccharomyces cerevisiae. Genetics 156, 579–592.

Mohapatra L, Goode BL, Kondev J (2015). Antenna mechanism of length control of actin cables. PLoS Comput Biol 11, e1004160.

Moseley JB, Goode BL (2005). Differential activities and regulation of Saccharomyces cerevisiae formin proteins Bni1 and Bnr1 by Bud6. J Biol Chem 280, 28023–28033.

Moseley JB, Maiti S, Goode BL (2006). Formin proteins: purification and measurement of effects on actin assembly. Methods Enzymol 406, 215–234.

Moseley JB, Sagot I, Manning AL, Xu Y, Eck MJ, Pellman D, Goode BL (2004). A conserved mechanism for Bni1- and mDia1-induced actin assembly and dual regulation of Bni1 by Bud6 and profilin. Mol Biol Cell 15, 896–907.

Okada K, Bartolini F, Deaconescu AM, Moseley JB, Dogic Z, Grigorieff N, Gundersen GG, Goode BL (2010). Adenomatous polyposis coli protein nucleates actin assembly and synergizes with the formin mDia1. J Cell Biol 189, 1087–1096.

Okada K, Ravi H, Smith EM, Goode BL (2006). Aip1 and cofilin promote rapid turnover of yeast actin patches and cables: a coordinated mechanism for severing and capping filaments. Mol Biol Cell 17, 2855–2868.

Paul AS, Pollard TD (2009). Review of the mechanism of processive actin filament elongation by formins. Cell Motil Cytoskeleton 66, 606–617.

Pruyne D, Gao L, Bi E, Bretscher A (2004). Stable and dynamic axes of polarity use distinct formin isoforms in budding yeast. Mol Biol Cell 15, 4971–4989.

Pruyne DW, Schott DH, Bretscher A (1998). Tropomyosin-containing actin cables direct the Myo2p-dependent polarized delivery of secretory vesicles in budding yeast. J Cell Biol 143, 1931–1945.

Rotty JD, Wu C, Haynes EM, Suarez C, Winkelman JD, Johnson HE, Haugh JM, Kovar DR, Bear JE (2015). Profilin-1 serves as a gatekeeper for actin assembly by Arp2/3-dependent and -independent pathways. Dev Cell 32, 54–67.

Sagot I, Klee SK, Pellman D (2002). Yeast formins regulate cell polarity by controlling the assembly of actin cables. Nat Cell Biol 4, 42–50.

Sambrook J, Fritsch EF, Maniatis T (1989). Molecular Cloning: A Laboratory Manual, Cold Spring Harbor, NY: Cold Spring Harbor Laboratory Press.

Schott D, Ho J, Pruyne D, Bretscher A (1999). The COOH-terminal domain of Myo2p, a yeast myosin V, has a direct role in secretory vesicle targeting. J Cell Biol 147, 791–808.

Sikorski RS, Hieter P (1989). A system of shuttle vectors and yeast host strains designed for efficient manipulation of DNA in Saccharomyces cerevisiae. Genetics 122, 19–27.

Suarez C, Carroll RT, Burke TA, Christensen JR, Bestul AJ, Sees JA, James ML, Sirotkin V, Kovar DR (2015). Profilin regulates F-actin network homeostasis by favoring formin over Arp2/3 complex. Dev Cell 32, 43–53.

Yang H-C, Pon LA (2002). Actin cable dynamics in budding yeast. Proc Natl Acad Sci USA 99, 751–756.

Yu JH, Crevenna AH, Bettenbühl M, Freisinger T, Wedlich-Söldner R (2011). Cortical actin dynamics driven by formins and myosin V. J Cell Sci 124, 1533–1541.